EPJ Web of Conferences **38**, 11002 (2012)
DOI: 10.1051/epjconf/20123811002

Evolution of nuclear properties in the long chain of Sn isotopes from A=100 to A=132

V. I. Isakov[1,a]

[1] Petersburg Nuclear Physics Institute, NRC Kurchatov Institute
188300 Gatchina, Russia

Abstract. This paper presents results of both microscopical and semi-empirical calculations of single-particle characteristics of nuclei and nuclear binding energies, as well as their root-mean-square radii, excitation energies and transition rates in the long chain of Sn isotopes, from the extremely neutron deficient ^{100}Sn up to neutron excess ^{136}Sn, where the experimental information is available by now. The comprehensive comparison with the experimental data is carried out.

Nuclear binding energies B, as well as one-nucleon separation energies S, are the major nuclear characteristics that define borders of nuclear stability and the decay modes of nuclei. Study of evolution of nuclear properties in the long chains of isotopes or isotones, from the extremely proton-excess up to the extremely neutron-excess nuclei is of special theoretical interest, as here one can check the adequacy of the used theoretical models in the broad interval of $(N-Z)/A$. Formerly, [1] we studied in details the chain of the $N = 82$ isotones. Different long chain is represented by the sequence of the nickel isotopes from ^{48}Ni up to ^{78}Ni, where all nuclei, except for ^{78}Ni, turn out to be discovered by the present time. The mentioned chain is of special interest as it includes doubly-magical nucleus ^{48}Ni (which is an extremely proton-excess one), and ^{78}Ni (the last one is strongly neutron-excess, and also the doubly-magical nucleus). This chain also includes doubly magical ^{56}Ni and semi-magical ^{68}Ni. The mentioned series of isotopes was theoretically analyzed by us in [2]. Another long isotopical chain is offered by the succession of tin isotopes having $Z = 50$. The experimental data are available from ^{102}Sn ($N = 52$) up to ^{136}Sn ($N = 86$). These nuclei are theoretically studied by us here.

For description of global properties of these isotopes we apply the Hartree–Fock–Bogoliubov method. We also use the approach based on the phenomenological mean field potential that was defined by us before [3]. This potential correctly takes into account isovector terms, which is very important when we consider long isotopical chains of nuclei. Here, we examine global properties of nuclei, such as their masses, root-mean-square radii of nucleon distributions, one- and two-nucleon separation energies, as well as single-particle energies of protons and neutrons. We also study excitation energies of nuclei, as well as the reduced transition rates as respect to the electromagnetic and weak transitions.

To define nuclear binding energies B in the self-consistent approach, we performed calculations based on the HF+BCS procedure that employs the Skyrme interaction and constant pairing with the corresponding proton and neutron pairing constants G_p and G_n to account for pairing correlations. In this case, one can represent the total energy of an even-even nuclei in its ground state in the following form, see the details in [4,5]:

$$E = -B = \int H_{\mathrm{HFBCS}}(\mathbf{r})\, d\mathbf{r} - \frac{\Delta_n^2}{G_n} - \frac{\Delta_p^2}{G_p}. \qquad (1)$$

Here and below, "n" refers to neutrons, while "p" to protons. Pairing correlations in the Hartree–Fock–Bogoliubov energy density $H_{\mathrm{HFBCS}}(\mathbf{r})$ were considered by introducing the occupancies v_i^2 into the single-particle density of matter, as well as into the kinetic energy and spin densities. In this way, the Hartree–Fock problem with modified densities was solved in coordinate representation, while the iteration procedure was applied for joint solution of the HF+BCS equations.

In our self-consistent calculations we used parameters of the Skyrme 3 interaction, while the pairing constants G were close to those from [6]. The exchange Coulomb terms were treated in the Slater approximation. In our calculations we considered all bounded single-particle levels as well as the quasi-stationary states.

One can see the values of the obtained binding energies for even isotopes of Sn in figure 1. In accordance with the experiment, the maximal binding energy per one nucleon happens for stable isotopes having $A \sim 124$.

In figure 2, we show both theoretical and empirical values of the two-neutron separation energies S_{2n} for the sequence of the even Sn isotopes. One can see the good agreement with the experiment. In particular, we observe rapid fractures of the values S_{2n} at $N = 82$ and $N = 50$, these fractures correspond to the closure of the corresponding neutron shells. Unfortunately, the mass of the $Z = 50, N = 48$ nucleus is unknown yet in the experiment. Note that we observe very small singularity of the curve at $N = 64$ (if at all). This is in contrast with the situation characteristic for isotones having $N = 82$, where one can see the visible fracture at $Z = 64$. This peculiarity, in aggregate with other experimental data, affords ground to consider ^{146}Gd as a nucleus having the features of the magical one [7].

[a] e-mail: visakov@thd.pnpi.spb.ru

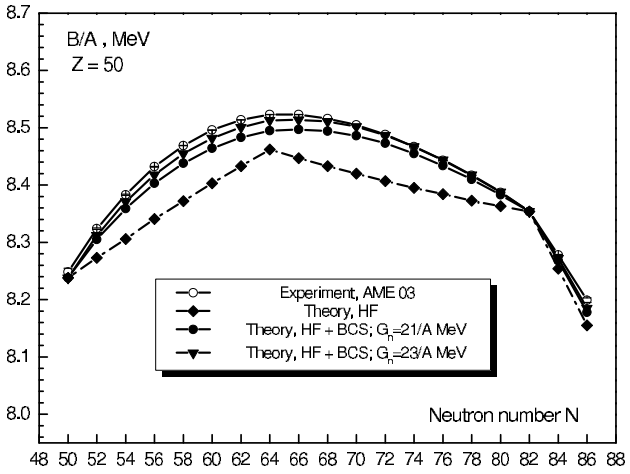

Fig. 1. Binding energies per nucleon B/A in the chain of the tin isotopes calculated with the standard Skyrme 3 and constant pairing interactions. All the experimental data concerning nuclear masses are from the Atomic Mass Evaluation (AME 03), see [8].

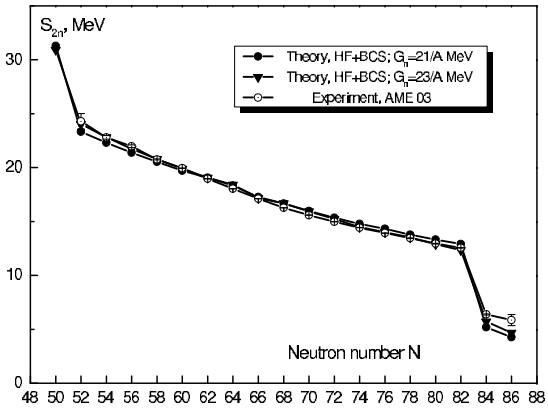

Fig. 2. Two-neutron separation energies S_{2n} in the chain of even tin isotopes. The calculations are performed within the HFBCS (Skyrme 3 + constant pairing) scheme.

Together with the self-consistent potential, we used also the phenomenological one. We defined this potential in [3], and it has the form

$$V(\mathbf{r},\sigma)=U\cdot f(r)+U_{ls}\cdot\frac{1}{r}\frac{df}{dr}\mathbf{l}\cdot\mathbf{s}\,;\;\; f(r)=\frac{1}{1+\exp((r-R)/a)}\,. \tag{2}$$

In Eq. (2), $U = V_0\left(1-\beta\frac{N-Z}{A}\cdot t_z\right)$, $U_{ls} = V_{ls}\left(1-\beta_{ls}\frac{N-Z}{A}\cdot t_z\right)$, $R = r_0A^{1/3}$, t_z=1/2 for neutrons and $t_z = -1/2$ for protons. In the case of protons we added to (2) the potential of a uniformly charged sphere with $R_c = r_cA^{1/3}$. The parameters of potential used here were as follows: $V_0 = -51.0$ MeV, $V_{ls} = 32.4$ MeV·fm^2, r_0=1.27 fm, r_c=1.25 fm, β=1.31, $\beta_{ls} = -0.6$, and $a = 0.6$ fm for both neutrons and protons. These parameters are very close to those from the paper [3].

In figure 3, we show evolution of the proton single-particle energies in the sequence of even tin isotopes as calculated by using the phenomenological and the self-consistent approaches. One can observe the similar behavior of the proton levels calculated in the framework of both schemes. We see that the energies of the proton single-particle levels decrease with the increase of the neutron number N when we approach the neutron drip line, this

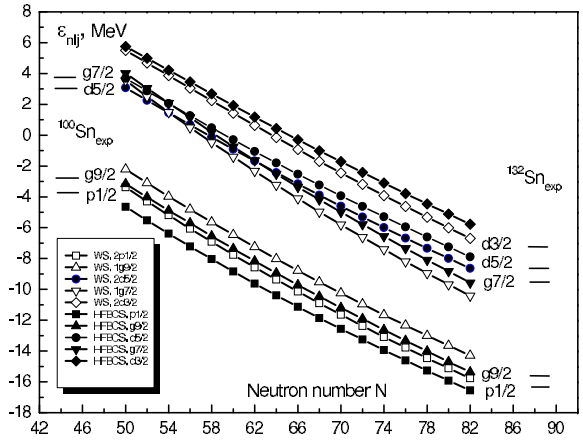

Fig. 3. Proton single particle energies ε_{nlj} in the chain of tin isotopes in the WS and the HFBCS schemes. The HFBCS procedure used the Skyrme 3 plus constant pairing interactions with $G_n = 21/A$ MeV.

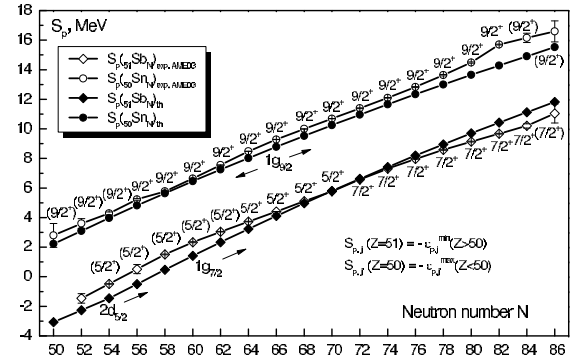

Fig. 4. Proton separation energies S_p in the chains of $Z = 51$ and $Z = 50$ isotopes as functions of the neutron number N calculated by using the phenomenological [3] WS scheme. Arrows show closest as respect to the gap single-particle proton orbit.

tendency is reproduced by the isotopical dependency of the central potential U in Eq. (2).

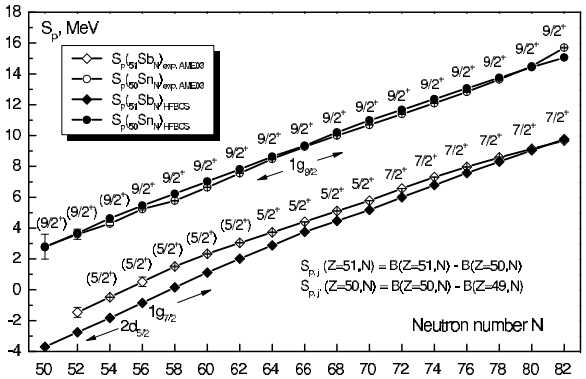

Fig. 5. Proton separation energies S_p for $Z = 51$ and $Z = 50$ calculated in the exact HFBCS method.

The comparison of the empirical and theoretical (WS) values of the one-proton separation energies S_p for the chains of isotopes $_{50}Sn_N$ and $_{51}Sb_N$ is shown in figure 4. The same comparison but for the HFBCS approach is represented in figure 5. We see that in both cases one can observe a good agreement with the experiment, this agree-

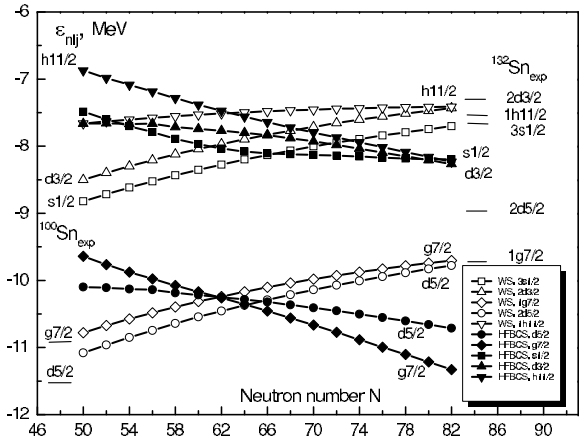

Fig. 6. Neutron single particle energies ε_{nlj} in the chain of tin isotopes calculated in the WS and the HFBCS (standard Skyrme 3 plus constant pairing interaction with $G_n = 21/A$ MeV) schemes.

ment is over the magnitudes of the separation energies as well as over the values of J^π for the isotopes with $Z = 49$ and $Z = 51$. One can see the existence of the large gap corresponding to the closure of the proton shell having $Z = 50$, for all values of N in the interval $50 \le N \le 82$.

In figure 6, we show evolution of the neutron single-particle levels for the succession of even isotopes of Sn. Here, one can see the striking difference between the forecasts as given by the WS and the HFBCS (Skyrme 3 + pairing) schemes. The neutron levels obtained in the framework of the self-consistent method do not follow the isotopical dependence of the central phenomenological potential (2). Self-consistent calculations show that by the approach to the neutron drip line bounded neutron levels close to the Fermi surface resist their extrusion into continuum. This gives a chance for existing very neutron-excess even Sn isotopes that are stable as respect to the neutron emission. Single-particle levels are not the observable ones, especially if we are far from the filled shells. So, let us compare the observable values, for example the one-neutron separation energies obtained in the frameworks of two methods. We show in figure 7 results of calculations of single-neutron separation energies $S_n(nlj)$ for a sequence of Sn isotopes in the framework of the phenomenological potential by using the ansatz:
$S_n(nlj)(N+1) = -\lambda_n(N) - E^{\min}_{nlj}(N+1)$ and
$S_n(nlj)(N-1) = -\lambda_n(N) + E^{\min}_{nlj}(N-1)$; N is even, while λ is chemical potential. Results of concurrent calculations, but performed in the HFBCS approach are shown in figure 8. Here, separation energies are found as differences of the corresponding binding energies. It is remarkably that both calculations lead to similar results and agree with the experiment.

By now, there exist large experimental information on the values of the root-mean-square charge radii of tin isotopes, the majority of information is obtained by means of methods of the laser spectroscopy. Thus, we performed corresponding calculations, both for protons and for neutrons. In Table 1 we show results of our calculations that were carried out in the self-consistent procedure by using both standard and modified (see below) Skyrme 3 schemes. Both calculations lead to close results. One can observe an agreement with experiment accurate within 0.3 %.

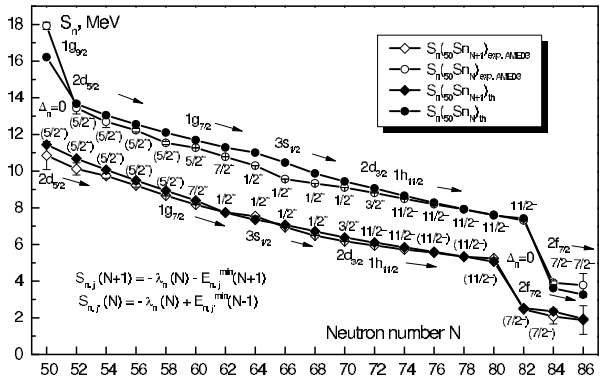

Fig. 7. Neutron separation energies S_n in the chain of tin isotopes calculated in the WS scheme.

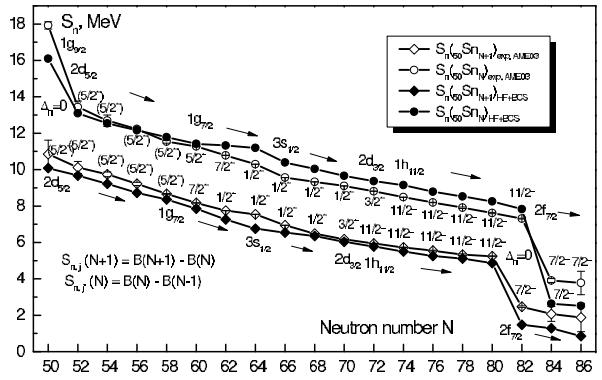

Fig. 8. Neutron separation energies S_n in the chain of tin isotopes calculated in the HFBCS approach (Standard Skyrme 3 + pairing with $G_n = 21/A$ MeV).

We also calculated proton and neutron density distributions for even isotopes of tin both in the standard Skyrme 3 + pairing, and in the WS schemes. The pattern of these distributions for the nuclei ^{120}Sn, that is close to the stability line is shown in figure 9. Both methods lead to close results.

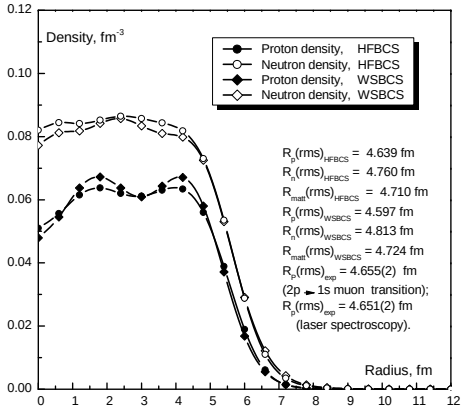

Fig. 9. Proton and neutron densities in ^{120}Sn in the WSBCS and the HFBCS schemes; $G_n = 21/A$ MeV.

For description of excited states and transition rates we used the QRPA approach [2], [9] with the phenomenological mean field potential shown by us before, as well as the effective interaction, the same in the particle–particle, particle–hole and pairing channels. For a system of only

Table 1. Root-mean-square radii R_p and R_n of the proton and the neutron distributions in the even isotopes of Sn, in the units of fm. Experimental data are borrowed from the electronic database [11] and from [12]. Calculations are performed by using the HFBCS method with the Skyrme 3 interaction and constant pairing having the standard value of the pairing constant [6], $G_n = 21/A$ MeV. Results of calculations performed by using the modified mean-field spin-orbital term are shown in square brackets.

N	$R(p)_{th}$	$R(p)_{exp}$	$R(n)_{th}$
50	4.464 [4.469]	–	4.387 [4.392]
52	4.484 [4.489]	–	4.434 [4.439]
54	4.503 [4.508]	–	4.478 [4.482]
56	4.521 [4.527]	–	4.519 [4.523]
58	4.540 [4.545]	4.558(3)	4.557 [4.560]
60	4.558 [4.563]	4.577(3)	4.594 [4.596]
62	4.575 [4.580]	4.594(2)	4.628 [4.630]
64	4.592 [4.596]	4.609(2)	4.662 [4.664]
66	4.609 [4.612]	4.624(2)	4.696 [4.697]
68	4.624 [4.628]	4.639(2)	4.728 [4.730]
70	4.639 [4.643]	4.651(2)	4.760 [4.762]
72	4.654 [4.658]	4.663(2)	4.791 [4.794]
74	4.668 [4.672]	4.673(3)	4.816 [4.819]
76	4.683 [4.686]	4.683(4)	4.840 [4.844]
78	4.696 [4.700]	4.692 6)	4.863 [4.867]
80	4.710 [4.714]	4.702(7)	4.884 [4.889]
82	4.724 [4.727]	4.709(8)	4.905 [4.909]
84	4.739 [4.742]	–	4.962 [4.950]

like particles and in a particle–particle channel this interaction coincides with the interaction used in the paper [10]. Our effective interaction $\hat{\vartheta}$ has the form

$$\hat{\vartheta} = \Big(V + V_\sigma \boldsymbol{\sigma}_1\boldsymbol{\sigma}_2 + V_T S_{12} + V_\tau \boldsymbol{\tau}_1\boldsymbol{\tau}_2 + V_{\tau\sigma}\boldsymbol{\sigma}_1\boldsymbol{\sigma}_2\cdot\boldsymbol{\tau}_1\boldsymbol{\tau}_2 + V_{\tau T} S_{12}\boldsymbol{\tau}_1\boldsymbol{\tau}_2 \Big) \exp(-r_{12}^2/r_{00}^2) + \frac{e^2}{r_{12}} \left(\frac{1}{2} - \hat{t}_z(1)\right)\left(\frac{1}{2} - \hat{t}_z(2)\right). \quad (3)$$

The entering parameters are as follows: $V = -16.65$, $V_\sigma = 2.33$, $V_T = -3.00$, $V_\tau = 3.35$, $V_{\tau\sigma} = 4.33$, $V_{\tau T} = 3.00$ (all these values are in MeV), while $r_{00} = 1.75$ fm.

Using the standard procedure, we can pass to the quasiparticle basis, $a^+ \to \xi^+$:

$$a^+_\alpha = u_{|\alpha|}\xi^+_\alpha - v_{|\alpha|}\varphi_\alpha \xi_{-\alpha}\,;\; u^2_{|\alpha|} + v^2_{|\alpha|} = 1\;;\varphi_\alpha = (-1)^{l_\alpha + j_\alpha - m_\alpha}. \quad (4)$$

Supposing the presence of correlations in the true ground state $|\tilde{0}\rangle$ of an even–even nuclei, we define the creation operator $Q^+_{n,JM}$ of the one-phonon excited state $|\omega_n, JM\rangle$ with $|\omega_n, JM\rangle = Q^+_{n,JM}|\tilde{0}\rangle$ in the following way:

$$Q^+_{n,JM} = \sum_{a\geq b} X^{n,J}_{j_a j_b} \left[\xi^+_a \xi^+_b\right]_{JM} - \sum_{c\geq d} Y^{n,J}_{j_c j_d} \left[\xi_c \xi_d\right]_{JM}, \quad (5)$$

where

$$\left[\xi^+_a \xi^+_b\right]_{JM} = \frac{1}{\sqrt{1+\delta_{j_a j_b}}} \sum_{m_a m_b} C^{JM}_{j_a m_a j_b m_b} \xi^+_{j_a m_a} \xi^+_{j_b m_b}, \quad (6)$$

$$\left[\xi_c \xi_d\right]_{JM} = \frac{1}{\sqrt{1+\delta_{j_c j_d}}} \sum_{m_c m_d} C^{JM}_{j_c m_c j_d m_d} \xi_{j_c - m_c} \xi_{j_d - m_d} \cdot \varphi_c \varphi_d, \quad (7)$$

$$X^{n,J}_{j_a j_b} = \langle \omega_n; JM | \left[\xi^+_a \xi^+_b\right]_{JM} |\tilde{0}\rangle,\; Y^{n,J}_{j_c j_d} = \langle \omega_n; JM | \left[\xi_c \xi_d\right]_{JM} |\tilde{0}\rangle. \quad (8)$$

In Eqs. (6), (7) and below $\delta_{j_a j_b} = \delta_{j_a j_b}\delta_{l_a l_b}\delta_{n_a n_b}$.

One may obtain the set of the QRPA equations which define the amplitudes "X" and "Y" of the states $|\omega_n, JM\rangle$ and the eigenvalues ω_n. These equations have the form

$$\left\| \begin{matrix} [(E-\omega)I + A] & B \\ -B & -[(E+\omega)I + A] \end{matrix} \right\| \times \begin{pmatrix} X \\ Y \end{pmatrix} = 0. \quad (9)$$

Here, $E = E_{ab} = E_{j_a} + E_{j_b}$, $I_{cd,ab} = \delta_{j_a j_c}\delta_{j_b j_d}$, while the matrix elements of the sub-matrices A and B in the case of even–even nuclei are as follows:

$$\begin{aligned} A_{cd,ab} \equiv A^J_{j_c j_d, j_a j_b} &= \left(u_{j_c}u_{j_d}u_{j_a}u_{j_b} + v_{j_c}v_{j_d}v_{j_a}v_{j_b}\right) \times \\ &\times {}_a\langle j_c j_d; J|\hat{\vartheta}|j_a j_b; J\rangle_a + \\ &+ \left(u_{j_c}v_{j_d}u_{j_a}v_{j_b} + v_{j_c}u_{j_d}v_{j_a}u_{j_b}\right) {}_a\langle j_c \bar{j}_d; J|\hat{\vartheta}|j_a \bar{j}_b; J\rangle_a + \\ &+ (-1)^{j_a+j_b+J+1}\left(v_{j_c}u_{j_d}u_{j_a}v_{j_b} + u_{j_c}v_{j_d}v_{j_a}u_{j_b}\right) \times \\ &\times {}_a\langle j_c \bar{j}_d; J|\hat{\vartheta}|j_b \bar{j}_a; J\rangle_a\,; \end{aligned} \quad (10)$$

$$\begin{aligned} B_{cd,ab} \equiv B^J_{j_c j_d, j_a j_b} &= \left(u_{j_c}u_{j_d}v_{j_a}v_{j_b} + v_{j_c}v_{j_d}u_{j_a}u_{j_b}\right) \times \\ &\times {}_a\langle j_c j_d; J|\hat{\vartheta}|j_a j_b; J\rangle_a - \left(u_{j_c}v_{j_d}v_{j_a}u_{j_b} + v_{j_c}u_{j_d}u_{j_a}v_{j_b}\right) \times \\ &\times {}_a\langle j_c \bar{j}_d; J|\hat{\vartheta}|j_a \bar{j}_b; J\rangle_a + (-1)^{j_a+j_b+J} \times \\ &\times \left(v_{j_c}u_{j_d}v_{j_a}u_{j_b} + u_{j_c}v_{j_d}u_{j_a}v_{j_b}\right) {}_a\langle j_c \bar{j}_d; J|\hat{\vartheta}|j_b \bar{j}_a; J\rangle_a. \end{aligned} \quad (11)$$

In Eqs. (10) and (11), ${}_a\langle j_c j_d; J|\hat{\vartheta}|j_a j_b; J\rangle_a$ and ${}_a\langle j_c \bar{j}_d; J|\hat{\vartheta}|j_a \bar{j}_b; J\rangle_a$ are the antisymmetric matrix elements of the effective interaction $\hat{\vartheta}$ in the particle–particle and particle–hole channels with a given spin. They have the form

$$\begin{aligned} {}_a\langle j_c j_d; J|\hat{\vartheta}|j_a j_b; J\rangle_a &= \frac{1}{\sqrt{(1+\delta_{j_c j_d})(1+\delta_{j_a j_b})}} \times \\ &\times \Big[\langle j_c j_d; J|\hat{\vartheta}|j_a j_b; J\rangle + (-1)^{j_a+j_b+J+1}\langle j_c j_d; J|\hat{\vartheta}|j_b j_a; J\rangle\Big], \end{aligned} \quad (12)$$

$$\begin{aligned} {}_a\langle j_c \bar{j}_d; J|\hat{\vartheta}|j_a \bar{j}_b; J\rangle_a &= -\frac{(-1)^{l_b+l_d}}{\sqrt{(1+\delta_{j_c j_d})(1+\delta_{j_a j_b})}} \times \\ &\times \sum_{J'} (2J'+1) W[j_b j_a j_c j_d; J J'] \times \\ &\times \Big[\langle j_b j_c; J'|\hat{\vartheta}|j_d j_a; J'\rangle + (-1)^{j_d+j_a+J'+1}\langle j_b j_c; J'|\hat{\vartheta}|j_a j_d; J'\rangle\Big]. \end{aligned} \quad (13)$$

Using an explicit form of the matrix equation (9), we obtain the orthonormality relation

$$\left| \sum_{a\geq b} X^{n,J}_{j_a j_b} X^{m,J}_{j_a j_b} - \sum_{c\geq d} Y^{n,J}_{j_c j_d} Y^{m,J}_{j_c j_d} \right| = \delta_{mn}, \quad (14)$$

which in terms of the QRPA bosons corresponds to the condition

$$\langle \omega_n, JM|\,\omega_m, JM\rangle = \langle \tilde{0}|Q_{n,JM}\cdot Q^+_{m,JM}|\tilde{0}\rangle = \delta_{mn}. \quad (15)$$

Considering the transition rates, we must distinguish between two different types of transitions, namely, transitions between the phonon states (i.e., between the two excited states), and the phonon–ground-state transitions. The latter transition is described by the reduced matrix element

$$\begin{aligned} \langle \tilde{0}||\mathcal{M}(\lambda)||\omega_n, J\rangle &= (-1)^\lambda \delta(J,\lambda)\delta(\pi_n\pi_\lambda) \times \\ &\times \Bigg[\sum_{j_a\geq j_b} X^{n,J}_{j_a j_b}(u_{j_a}v_{j_b} \pm v_{j_a}u_{j_b}) \frac{(-1)^{l_b}}{\sqrt{1+\delta_{j_a j_b}}} \langle j_a||\hat{m}(\lambda)||j_b\rangle - \\ &- \sum_{j_a\geq j_b} Y^{n,J}_{j_a j_b}(v_{j_a}u_{j_b} \pm u_{j_a}v_{j_b}) \frac{(-1)^{l_b}}{\sqrt{1+\delta_{j_a j_b}}} \langle j_a||\hat{m}(\lambda)||j_b\rangle \Bigg], \end{aligned} \quad (16)$$

where the upper signs refer to T-even (Eλ), while the lower ones to T-odd (Mλ) transitions.

One can show that the "phonon–phonon" matrix element has the form

$$\langle \omega_n, J' \| \hat{\mathcal{M}}(\lambda) \| \omega_m, J \rangle = [(2J+1)(2J'+1)]^{1/2} \times$$
$$\times \sum_{j_a \geq j_b, j_c \geq j_d} \frac{\left[X^{m,J}_{j_a j_b} X^{n,J'}_{j_c j_d} \pm Y^{m,J}_{j_a j_b} Y^{n,J'}_{j_c j_d} \right]}{\sqrt{(1+\delta_{j_a j_b})(1+\delta_{j_c j_d})}} \times \qquad (17)$$
$$\times \Big\{ \delta_{j_b j_d} W[\lambda j_c J j_b; j_a J'] (u_{j_c} u_{j_a} \mp v_{j_c} v_{j_a}) \langle j_c \| \hat{m}(\lambda) \| j_a \rangle -$$
$$- (-1)^{j_c + j_d + J'} \delta_{j_b j_c} W[\lambda j_d J j_b; j_a J'] (u_{j_d} u_{j_a} \mp v_{j_d} v_{j_a}) \times$$
$$\times \langle j_d \| \hat{m}(\lambda) \| j_a \rangle - (-1)^{j_a + j_b + J} \delta_{j_a j_d} W[\lambda j_c J j_a; j_b J'] \times$$
$$\times (u_{j_c} u_{j_b} \mp v_{j_c} v_{j_b}) \langle j_c \| \hat{m}(\lambda) \| j_b \rangle + (-1)^{j_a + j_b + J + j_c + j_d + J'} \times$$
$$\times \delta_{j_a j_c} W[\lambda j_d J j_a; j_b J'] (u_{j_d} u_{j_b} \mp v_{j_d} v_{j_b}) \langle j_d \| \hat{m}(\lambda) \| j_b \rangle \Big\},$$

where the upper signs refer to Eλ, while the lower ones – to Mλ transitions. In figure 10, we show systematics of experimental and theoretical energies of the first quadrupole and octupole states in the sequence of N-even isotopes of Sn, while figure 11 demonstrates the comparison of theoretical and experimental values of $B(E2)$. For magical nuclei we also show here fractions of the corresponding transition rates as compared to the total sum rule. One can find results of alternative calculations in the paper [13]. Here we used values of corresponding effective charges defined by us before in description of the $E2$ transitions in the vicinities of ^{208}Pb and ^{132}Sn. Similar comparison, but for the $E3$ transitions is shown in figure 12. One should mention here previous calculations [14–16] performed for nuclei where the experimental information is available.

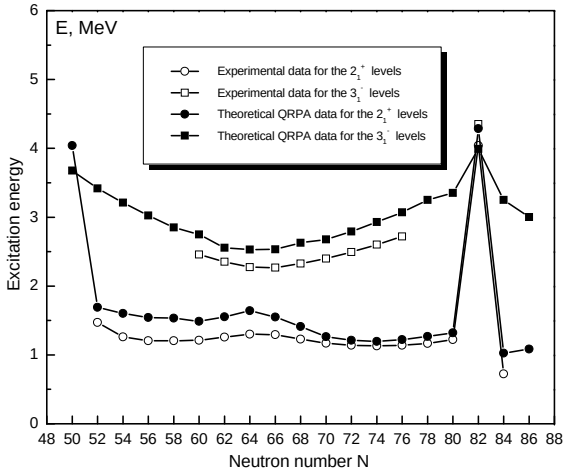

Fig. 10. Experimental and theoretical energies of the 2^+_1 and 3^-_1 states in even isotopes of Sn. Our basis included 10 proton and 15 neutron single-particle levels.

Results of the more detailed calculations for ^{130}Sn are shown in figure 13. Here we also show results of our RPA calculations obtained by solution of the Bethe–Salpeter equation in media. Results of the analogous calculations, but for ^{102}Sn are shown in figure 14. By now, there exist two sets of experimental data pertinent to ^{102}Sn, namely [17], and [18]. Being strongly different from each other, they both lead to anomalously large values of the effective neutron charge as defined from the 6^+ to 4^+ transition.

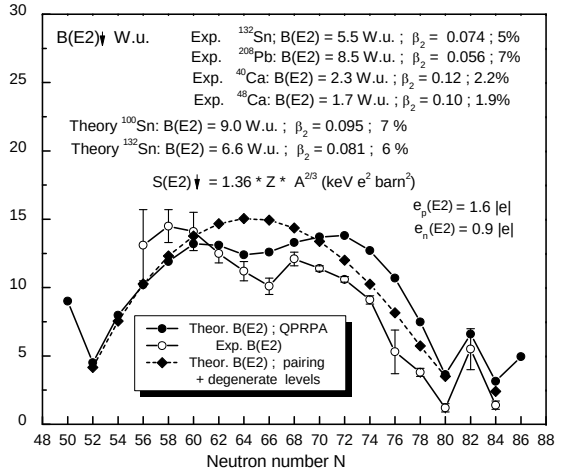

Fig. 11. Reduced transition rates from the 2^+_1 states in even isotopes of Sn. Dashed line shows results of calculations performed by using only degenerate neutron levels of the 50–82 shell and the pairing interaction. The corresponding curve line (parabola) is normalized to theoretical (QRPA) transition rate in ^{130}Sn. The sum rule evaluation corresponds to the uniform charge distribution with $R = 1.2\,A^{1/3}$ fm. Experimental data are borrowed from the papers [19]–[24].

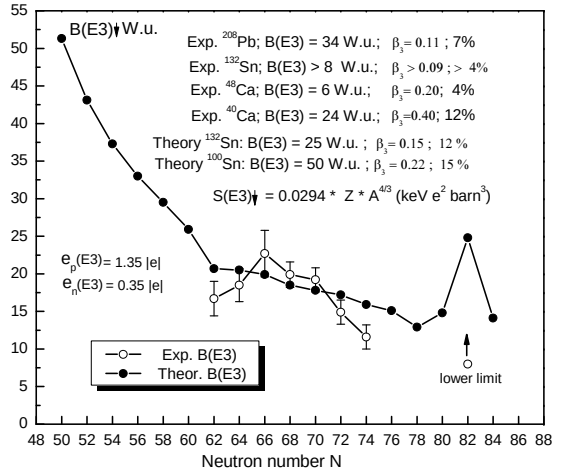

Fig. 12. Reduced transition rates from 3^-_1 states in even isotopes of Sn. The experimental data are from [25].

The structure of the lowest states in ^{102}Sn strongly depends on the mutual disposition of the neutron $d_{5/2}$ and $g_{7/2}$ states, and is sensitive to the spin-orbit splitting. In the Skyrme scheme this splitting is generated by the parameter W, that defines the strength of the two-body spin-orbit interaction. At the same time, some spin-orbit splitting arises also from the spin-density term, which is usually ignored in the Skyrme single-particle equations. The contribution of this term into splitting is proportional to

$$(t_1 - t_2) \sum_{j_\alpha} v^2_{j_\alpha} (2j_\alpha + 1) \left[j_\alpha (j_\alpha + 1) - l_\alpha (l_\alpha + 1) - \frac{3}{4} \right] R^2_{j_\alpha}(r), \qquad (18)$$

where t_1 and t_2 are the Skyrme force parameters.

As the radial wave functions of the spin-orbital doublet are very close to each other, one can easily see that contributions from filled levels of the spin-orbital doublet mutually contract each other, if the core is the spin-saturated one (for example, ^{40}Ca). In the case of nuclei just above ^{100}Sn the non-zero contribution to splitting arises only from the

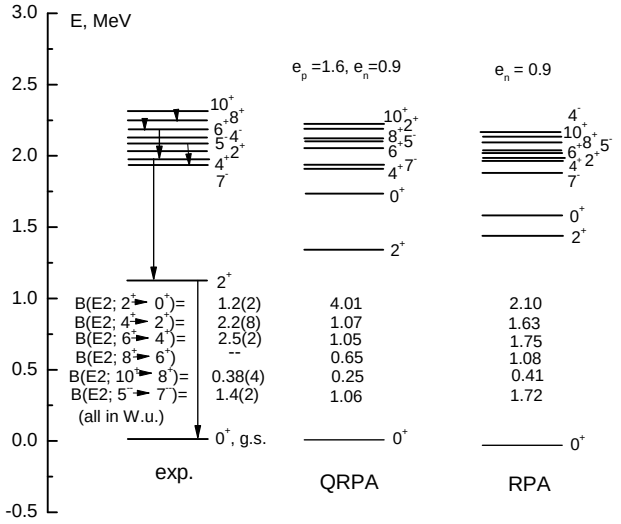

Fig. 13. Spectra of levels and transition rates in ^{130}Sn. The experimental data are from [26] and [27].

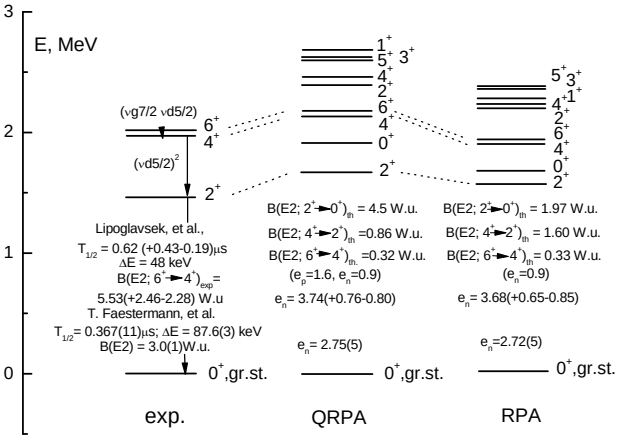

Fig. 14. Structure of levels and transition rates in ^{102}Sn. Leading configurations shown in the figure correspond to the case, when the neutron $2d_{5/2}$ state is lower than the $1g_{7/2}$ one.

filled $1g_{9/2}$ proton and neutron sub-shells, this contribution is small and of the opposite sign as compared to that mediated by the spin-orbit two-body interaction. However, we also performed calculations with inclusion of the spin-density term into the corresponding single-particle equations. The results are shown in figure 15, from which we see that here the spin-orbital splitting really decreases a little, with the main effect of variation of the mutual disposition of the neutron $d_{5/2}$ and $g_{7/2}$ levels in even isotopes of Sn close to $A = 100$. Here, the neutron $g_{7/2}$ level proves to be lower than the $d_{5/2}$ one, this difference may be important for description of the electromagnetic transition rates in these nuclei. One can observe the same pattern for the proton levels. It is very important that such modification of the Skyrme single-particle potential in practice does not influence the results of calculations shown in figures 1, 2, and figure 8. The influence of this term on the values of the root-mean-square radii is also small, as one can see from Table 1. We note here that spin-density terms, by their impact on binding energies and on the spin-orbital splitting, in a way simulate the two-body tensor interaction. Our calculations show that the reasonable variation of the mutual disposition of the $d_{5/2}$ and $g_{7/2}$ states may really lead to some increase of the $B(E2; 6_1^+ \to 4_1^+)$ in ^{102}Sn, but in any

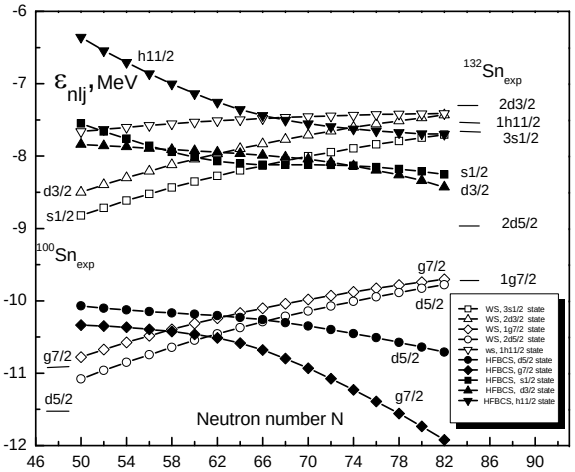

Fig. 15. Neutron single particle energies ε_{nlj} in the chain of even isotopes of tin calculated in the WS and the HFBCS approaches (with modified Skyrme 3 scheme).

case the value of the neutron effective charge is more than 2. At the same time, the available experimental data manifest [28] that in nuclei close to ^{100}Sn the $d_{5/2}$ state is the lowest one.

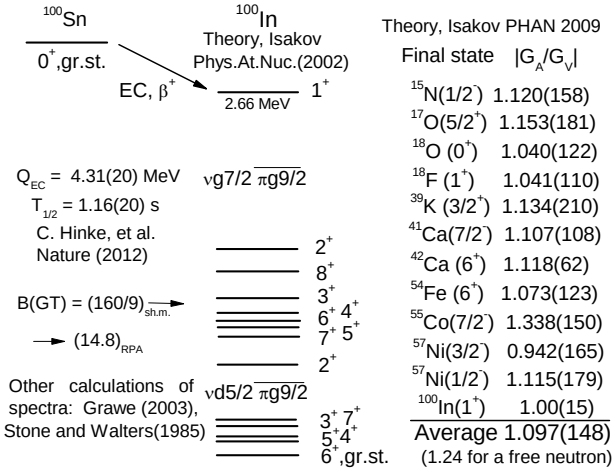

Fig. 16. Structure of levels and EC/β^+ transition rate in ^{100}In.

Authors of the recent paper [29] carefully measured Q_{EC} and $T_{1/2}$ for the very strong Gamow–Teller transition from 0^+ (g.s., ^{100}Sn) to 1^+ in ^{100}In. This gives us the opportunity to define the $|G_A/G_V|$ ratio for this transition. The comparison of the obtained result with the results of our our recent calculations [30] performed for other $N \sim Z$ nuclei are shown in figure 16. We see that the renormalization of the G_A constant in nuclei as compared to that in the decay of a free neutron is very small. Note that in our calculation for the decay of ^{100}Sn we did not take into consideration fragmentation of the $\pi g_{9/2}$ and $\nu g_{7/2}$ states, this fragmentation is not known in the experiment in nuclei close to ^{100}Sn. However, we considered similar effects in other nuclei. The account of this fragmentation will lead to a further small increase of the $|G_A/G_V|$ ratio in the decay of ^{100}Sn.

In our calculations, in the framework of the spherical scheme we considered global properties of tin isotopes in the large interval of the neutron number N, from the

neutron-deficient ^{100}Sn up to the neutron-excess ^{132}Sn. For description of different nuclear properties we used more-or-less standard methods, as well as previously defined entering parameters, and obtained results that are mainly in agreement with the experiment.

Our results show that the neutron $d_{5/2}$ and $g_{7/2}$ states of the 50 − 82 shell are separated from the $h_{11/2}$, $d_{3/2}$ and $s_{1/2}$ ones. It exhibits in the downfall of the $B(E2; 2_1^+ \to 0_1^+)$ values and in a small raising of the $E(2_1^+)$ energies at $N \sim 64$, both effects are seen in the experiment. At once we do not see the fracture of the S_{2n} values at $N = 64$.

We notice that the value of the neutron effective charge defined from the $6_1^+ \to 4_1^+$ transition in ^{102}Sn is abnormally large. At the same time, it was shown in [31] that by using the experimental value [32] of $B(E2; 8_1^+ \to 6_1^+)$ in ^{98}Cd, we obtain the anomalously small value of the proton effective charge. One may conventionally assume the presence of strong superfluid correlations in nuclei just close to ^{100}Sn. This results in suppression of the transition matrix elements between the two-quasiparticle states in ^{98}Cd due to the factor $(u_1u_2 - v_1v_2)$, and thus leads to the increase of the proton effective charge. However, we are unable to explain in this way experimental data in ^{102}Sn. For a while we do not have satisfactory quantitative explanation of abnormal values of the effective charges.

Our calculations denote that the quenching of the $M1$ transition rates in nuclei against those calculated with the bare value of G_A is small.

Acknowledgement

This work was performed under the support of the Russian Foundation for Basic Research (grant no. RSGSS-65751.2010.2).

References

1. K.I. Erokhina, V.I. Isakov, B. Fogelberg *et al.*, Part. and Nucl. Lett. No. 4 (**107**), 5 (2001)
2. V.I. Isakov, Phys. At. Nucl. **73**, 1515 (2010)
3. V.I. Isakov, K.I. Erokhina, H. Mach *et al.*, Eur. Phys. J. A **14**, 29 (2002)
4. V. I. Isakov, K. I. Erokhina, B. Fogelberg *et al.*, Part. and Nucl. Lett. No. 5 **102**, 44 (2000)
5. D. Vautherin and D. M. Brink, Phys. Rev. C **5**, 626 (1972)
6. V.G. Soloviev, *Theory of Complex Nuclei* (Pergamon Press, Oxford, 1976)
7. S.A. Artamonov, V.I. Isakov, Yu.N. Novikov *et al.*, Part. and Nucl. **20**, No. 2, 440 (1989)
8. G. Audi, A.H. Wapstra, and C. Thibault, Nucl. Phys. A **729**, 337 (2003)
9. M. Baranger, Phys. Rev. **120**, 957 (1960)
10. K. Heyde and M. Waroquier, Nucl. Phys. A **167**, 545 (1971)
11. I.N. Boboshin, V.V. Varlamov, Yu.P. Gangrsky *et al.*, http://cdfe.sinp.msu.ru/services/radchart/radmain.html
12. I. Angeli, At. Data Nucl. Data Tables **87**, 185 (2004)
13. N. Lo Iudice, Ch. Stoyanov, and D. Tarpanov, Phys. Rev. C **84**, 044314 (2011)
14. V. Gillet, D. Giraud, and M. Rho, Phys. Rev. **178**, 1695 (1969)
15. A.P. Severyukhin, V.V. Voronov, Ch. Stoyanov, and N. Van Giai, Phys. At. Nucl. **66**, 1434 (2003)
16. A.P. Severyurhin, V.V. Voronov, and N. Van Giai, Eur. Phys. J. A **22**, 397 (2004)
17. M. Lipoglavsek, D. Seweryniak, C.N. Davids *et al.*, Phys. Lett. B **440**, 246 (1998)
18. T. Faestermann, Private communication; http://www.nscl.msu.edu/ brown/EFES-2010/pdf/ faestermann.pdf
19. S. Raman, C.W. Nestor Jr., and P. Tikkanen, At. Data Nucl. Data Tables **78**, 1 (2001)
20. D.C. Radford, C. Baktash, J.R. Beene *et al.*, Eur. Phys. J. A **25**, Suppl. 1, 383 (2005)
21. R.L. Varner *et al.*, Eur. Phys. J. A **25**, Suppl 1, 391 (2005)
22. J. Cedercäll, A. Ekström, C. Fahlander *et al.*, Phys. Rev. Lett. **98**, 172501 (2007);*EGP Workshop* (Paris, 2008)
23. A. Ekström, J. Cedercäll, C. Fahlander *et al.*, for the IS418 Collaboration, *ISOLDE Workshop* (CERN 17–19 Dec., 2007)
24. A. Jungclaus, J. Walker, J. Leske *et al.*, Phys. Lett. B **695**, 110 (2011)
25. R.H. Spear, A.M. Baxter, S.M. Burnett, and C.L. Miller, At. Data Nucl. Data Tables **42**, 55 (1989)
26. http://www-nds.iaea.or.at
27. K.I. Erokhina, V.I. Isakov, B. Fogelberg, and H. Mach, Preprint PNPI-2225 (Gatchina 1998)
28. D. Seweryniak, M.P. Carpenter, S. Gross *et al.*, Phys. Rev. Lett. **99**, 022504 (2007)
29. C.B. Hinke, M. Bohmer, P. Boutachkov *et al.*, Nature **486**, 341 (2012)
30. V.I. Isakov, Phys. At. Nucl. **72**, 33 (2009)
31. V.I. Isakov and K.I. Erokhina, Phys. At. Nucl. **65**, 1431 (2002)
32. M. Górska, M. Lipoglavsek, H. Grawe, *et al.*, Phys. Rev. Lett. **79**, 2415 (1997)